Shear-driven segregation of dense granular mixtures in a split-bottom cell

Yi Fan and K. M. Hill
St. Anthony Falls Laboratory, Department of Civil Engineering, University of Minnesota, Minneapolis, Minnesota 55414, USA
(Received 8 January 2010; published 14 April 2010)

Shear-driven segregation of dense granular mixtures has been associated with a number of interesting pattern formation problems. We use experimental and computational split-bottom cells to isolate segregation effects associated with shear gradients from those associated with gravity. We find the effect of shear gradients much less dramatic than initial observations of segregation suggest. While a segregation pattern emerges in a circular split-bottom cell that appears coincident with the shear gradient, we find the pattern is orthogonal to the active segregation flux. We measure a toroidal convection roll that, in conjunction with gravity-driven segregation, is likely responsible for the dramatic horizontal segregation pattern. On the other hand, computational results from a parallel split-bottom cell indicate a subtle segregation flux associated with the shear gradient. The nature of the driving mechanism is unknown. A current predictive form of kinetic theory based on binary collisions dominating the particle dynamics predicts segregation in the opposite direction from observed trends. This indicates the direction of shear-driven segregation depends on the nature of the flow itself, collisional or frictional.

DOI: 10.1103/PhysRevE.81.041303 PACS number(s): 45.70.Mg, 45.70.Qj, 47.57.Gc, 81.05.Rm

I. INTRODUCTION

Particle mixtures will self-sort by size, density, and other particle property when disturbed. This is an important problem for industries that need to have particles well-mixed or, at the very least, need a method for predicting the local distribution when they will not be well-mixed. In systems of higher solids fraction, gravity-driven segregation has been well documented in dense sheared granular flow [1,2]. This has led to segregation patterns ranging from snout formation in debris flows [1] to radial segregation [3] and more complex segregation patterns [4] in a rotating drum.

There have been a number of modeling techniques used for gravity-induced segregation in dense systems [1,3,5]. The most successful *predictive* formulation involves an empirical segregation model superposed on a continuum model for the average flow [1–4]. However, this method depends on an accurate segregation model. For segregation arising from gravity (often associated with kinetic sieving and squeeze-expulsion mechanisms as in [5]), a model for segregation for particle size has been derived based on a distribution of pressures within a mixture that depends on particle size by Gray and colleagues [1,2]. Despite evidence of shear-associated segregation effects in both dilute and dense granular mixtures, there is no shear-driven segregation model analogous to the one for gravity-driven segregation for dense flows. Further, reports of shear-induced segregation effects in dense sheared flows are contradictory, with some reports of large particles gathering in high shear regions [6,7] and some reports of large particles repelled from high shear regions [8].

In contrast, reports of shear-induced segregation effects in dilute energetic granular mixtures are quite consistent. Physical and computational experiments show effects related to a shear gradient drive *all* particles to regions of low shear rate, though the larger particles are driven there faster, thus segregating from the mixture (e.g., [9–11]). Within the framework of kinetic theory, several have derived explicit expressions for segregation in terms of external forces (e.g., gravity) and interactions between particles that depend explicitly only on the gradient of granular temperature, species concentrations, and particle properties (e.g., size and density) [12–19]. In the case of sheared granular mixtures, the shear gradient and boundary effects give rise to a granular temperature gradient, i.e., a gradient in the kinetic energy associated with the variance of the velocities. Kinetic theory successfully models the segregation according to granular temperature gradient associated with the shear gradient. However, Xu *et al.* [11] showed that kinetic theory overestimates segregation once the solids fraction is significantly more than 30% and likely needs be modified to better model segregation in denser systems. We address these limitations in our analysis and in the summary section.

In concentrated suspensions and slurries, where both particle-particle and particle-fluid interactions are important, reports of shear-induced segregation effects are similar to those from sparse dry granular mixtures. Specifically, *all* particles migrate to regions of lower shear rate [20,21], while larger particles segregate to the region of lower shear rate faster [22]. Leighton and Acrivos [20,21] developed a theoretical framework for the migration process, later modified to account for the curvature-induced migration observed by Krishnan *et al.* [23]. In contrast with kinetic theory, a statistical model based on binary particle collisions, they developed a macroscopic shear-induced diffusion model, where the diffusion coefficient depends both on local shear rate and particle size. The general prediction from both frameworks is the same, however, with large particles migrating to a region of lower shear rate. Results are similar for a granular slurry, where particles are denser than the interstitial fluid. Barentin *et al.* [24] attributed the segregation in slurries to the same shear-induced diffusion effect proposed by Krishnan *et al.* [23].

While there have been relatively consistent reports for shear-induced segregation of different-sized particles in dilute dry systems and in suspensions and slurries, the reports of analogous segregation in dry dense granular mixtures are somewhat more varied. Bridgwater and colleagues per-

formed some of the earliest experiments used to study shear-induced size segregation in dry dense granular mixtures [6,7,25]. They found that in an annular shear cell where the shear is greatest in the middle of the cell [6], large particles move to the region of highest shear rate, directly opposite the trend observed in dilute systems, in suspensions, and in slurries. They found similar results in a reciprocating simple shear cell with flexible walls [7]. Whether the shear gradient increased or decreased in the direction of gravity, they found that the large particles moved to the region of larger shear rate. Bridgwater attributed the shear-induced segregation to the gradient of solids fraction induced by the shear gradient. They hypothesized that the higher shear rate gave rise to a higher frequency of voids, increasing the diffusive motion of large particles to a higher shear rate [6,7].

Other observations of segregation in dense flows have been associated shear gradients and granular temperature gradients. Recently, Rietz and Stannarius [8] studied the kinematics of mixtures and their segregation properties in a long thin rectangular box rotated horizontally about its long axis. In these systems, the authors reported persistent convection rolls in the plane of the box and segregation patterns associated with these convection rolls. In this case, small particles accumulated on the outer edge of the convection rolls, associated with the largest shear gradients in the system, in contrast to the segregation observations reported by Bridgwater and colleagues [6,7]. In another rotating system, this a long horizontal drum, Zuriguel *et al.* [26] studied the dynamics of relatively few large particles in a matrix of small particles when rotated in a long horizontal drum. In this case, the proximity of large particles altered the local velocity and granular temperature gradients, which themselves gave rise to segregation effects that varied with the rotation speed of the drum. At lower speeds, the proximity of two large particles resulted in a region of relatively low granular temperature between them. The large particles then migrated to this low temperature region, segregating from the small particle matrix. The dynamics reversed at higher speeds when the temperature gradients were small.

To summarize, while many have observed rather consistent shear-induced segregation trends in sparse dry granular systems, suspensions and slurries, to this point, shear-induced segregation trends in denser dry systems appear somewhat inconsistent. Further, there is no clear physical or mathematical framework to explain how the gradient of shear rate may give rise to size segregation in dense flow, whether there is a single mechanism such as a gradient in granular temperature or pressure, or whether there are multiple mechanisms which dominate for different phases of granular flow. Part of the difficulty in developing an appropriate theory lies in the lack of an appropriate geometry for isolating shear gradients from other segregation effects. In typical experimental systems designed to study segregation in dense granular flow such as chutes and rotated drums, gravity, velocity gradients, and porosity gradients (and other effects) coexist in the direction of segregation.

In this paper, we describe physical and computational experiments used to study shear-induced segregation in dense sheared mixtures in a split-bottom cell. The split-bottom cell gives rise to a shear gradient and associated temperature gradient normal to gravity. In Sec. II we describe our observations of segregation parallel to the shear gradient in an experimental split-bottom cell. In Sec. III we describe our computational experiments designed to study shear-induced segregation effects in split-bottom cells with and without curvature and to better understand the kinematics associated with these segregation observations. In Sec. IV, we compare some predictions from the framework of kinetic theory to our segregation results. We will conclude with a summary and discussion in Sec. V.

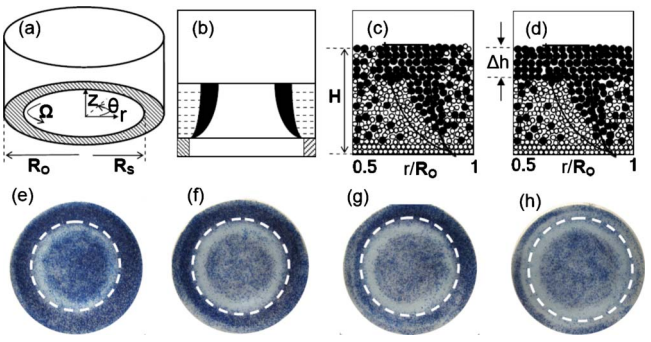

FIG. 1. (Color online) Experimental apparatus and bulk segregation. (a) Sketch of the experimental circular split-bottom cell. (b) Sketch of a vertical and radial cross section of a typical experiment, where the shear zone is indicated by the darkened region. (c) Sketch of the final bulk segregation pattern in a binary mixture of different-sized particles after 300 revolutions of the base. (d) The same as (c), though the initial conditions include a cap of the larger particles of thickness Δh on top of the mixture. (e)–(h) Photographs taken at various depths of a system of 1 mm (white) and 2 mm (dark, or blue online) glass beads after an experiment such as that shown in Fig. 1(d) is performed, where $H=55$ mm, and $\Delta h=15$ mm. The pictures are taken after 300 revolutions of the base for heights above the bottom (e) $z=40$ mm; (f) $z=30$ mm; (g) $z=20$ mm; (h) $z=10$ mm. The dashed lines represent the center of shear zone at each height, also the region of highest shear rate, as calculated using Eq. (1).

II. PHYSICAL EXPERIMENTS

Our experimental apparatus is the circular split-bottom cell described previously in Ref. [27] [see Fig. 1(a)]. In this system, the gradient of the shear rate is primarily perpendicular to gravity. The outer radius of our cell $R_o=145$ mm, and the base is split at radius $r=R_s=121$ mm. The outer part of the base is fixed to the vertical cylinder walls, and the inner disk rotates at an angular velocity $\Omega=0.01$ rev/sec. The boundary friction is controlled using a layer of 2 mm glass particles glued to the base of the cell. We fill the cylinder with particles to a height $H \leq 0.45R_s$. As first shown in Ref. [28], at these filling levels, a cylindrically symmetric, vertical shear band is produced in the bulk of the granular materials. Near the base the shear band is narrow and centered at the split; with increasing distance from the bottom z, the band shifts inward slightly, and its width increases [Fig. 1(b)]. At any particular distance from the base of the cell z, the angular velocity profiles can be fit by an error function, and the shear rate is largest at the middle of the shear band

$R_c(z)$ [29–31], where Unger *et al.* [32] showed

$$z = H - R_c\{1 - R_s/R_c[1 - (H/R_s)^{2.5}]\}^{0.4}. \quad (1)$$

Previously [27], we found that when mixtures of different-sized particles were sheared as described above, the large particles segregated to the top of the shear band within a few rotations forming a cap of segregated large particles of thickness approximately ten times the average particle diameter in the mixture. The rest of the shear band remains mixed over a longer period of time (10's of rotations). We then changed the initial conditions to one where the mixture was capped with large particles of a thickness approximately ten times the average particle diameter in the mixture. In this way, we moved any surficial effect on segregation away from the mixture. In this case, the mixture did not appear to segregate. We attributed these observations to the possibility that vertical segregation driven by gravity was facilitated by large porosity or porosity gradients, without which gravity-driven segregation will be greatly slowed or eliminated. In both cases, this leaves a mixture in the bulk sheared primarily in the horizontal direction.

To investigate segregation driven by horizontal shear gradients within the bulk we perform both types of experiments described above (with and without the cap of large particles atop the mixture) for a much longer duration using binary mixtures of glass particles of diameters 1, 2, or 3 mm. We investigate the evolution of segregation in the bulk by running several consecutive experiments of increasing duration. After each run of progressively longer duration (of approximately 1/2 hour intervals), we remove the layers of particles incrementally and note the segregation state at each depth as in Ref. [27]. Then we remix the particles and restart the experiment. Each run is repeated at least three times to assure reproducibility of experimental results.

After approximately thirty revolutions, in addition to vertical segregation, the particles within the bulk begin to segregate in the radial direction, in other words, in the direction of the horizontal shear gradient. A cylindrical shell of small particles forms within the shear band at smaller radii, and a band of large particles occupies the outer part of the shear band. This horizontal segregation is a much slower process than vertical gravity-driven segregation and appears to reach a steady state after over one hundred revolutions. The final segregation patterns from the two types of experiments, with and without the initial cap of large beads, are sketched in Figs. 1(c) and 1(d).

Figure 1(e)–1(h) are photographs taken from above one experiment (such as that illustrated in Fig. 1(d)) during the bulk excavation process. Heights for each are specified in the figure caption. For the top three positions [Figs. 1(e)–1(g)], there are four cylindrical shells of different phases of the mixture: at smaller radii where the shear rate is negligible during the experiment, the system remains mixed. At intermediate radii, a lighter band of small particles is noticeable. At larger radii, a darker band of larger particles is visible in the region of the shear band, and at the largest radii, adjacent to the outer wall, the system is mixed. At the lowest position [Fig. 1(h)] very few large particles are visible, presumably due to vertical segregation of the large particles away from the bottom. At this point, we only see small particles throughout the shear band and only the mixed phase in the inner and outer region.

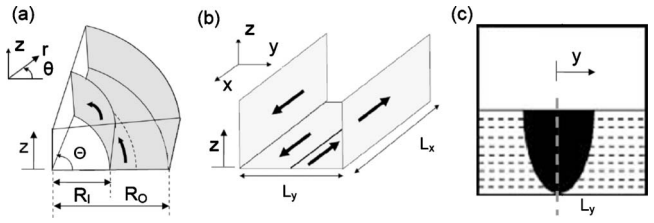

FIG. 2. Sketches of the setup for the simulations. (a) Circular split-bottom cell. (b) Parallel split-bottom cell. (c) Sketch of a cross section of a typical computational experiment in the parallel cell. The shear zone is indicated by the darkened region.

Dashed lines shown in Figs. 1(e)–1(h), denote the centers of shear zone, the region of the highest shear, as calculated by Eq. (1). We note that rather than indicating that the small particles or large particles segregate to a higher or lower shear rate, these results indicate that the bands of small and large particles are separated approximately by R_c, the location of the highest shear rate.

While the horizontal segregation patterns in our experiments indicate shear-induced segregation patterns, the results are markedly different from previous observations of shear-induced size segregation in dense flow. In our system, the highest shear rate marks the border between segregated small and large particles. Others have found either large [6,7] or small [8] particles segregate to higher shear rate. To more easily investigate the reasons for these discrepancies, we use computational simulations where more detailed information such as the species concentrations, velocities, and granular temperatures are available.

III. COMPUTATIONAL EXPERIMENTS

We use the discrete (or distinct [33]) element method (DEM) with a "soft sphere" interparticle force model [34,35] in our computational experiments. The particles are 2 and 3 mm spheres with similar properties to glass, though they are softened slightly reduce the computational time [36]. To avoid crystallization, the radii of each size of particle are slightly polydisperse (10% of the average radii). We perform computational experiments in two geometries, illustrated in Figs. 2(a) and 2(b). The first, a circular split-bottom cell [Fig. 2(a)] is similar to the experiment, but an inner wall is used to reduce computational cost and to avoid a singularity problem in the center of cylinder. The radius of inner wall $R_i = 95$ mm. Additionally, only a sector of the circular split-bottom cell is simulated; the boundaries are periodic in the azimuthal direction. The solid angle Θ was chosen to be large enough so the results were not influenced by this: $\Theta = 12°$. The outer radius R_o and the radius of the split R_s are the same as those in the experiments: $R_s = 121$ mm and $R_o = 145$ mm. The ratio between the radius of the inner and outer walls R_i/R_o is similar to that in Refs [28,29].

The second geometry simulated is a parallel split-bottom cell [Fig. 2(b)], similar to that of Ries *et al.* [38]. In this

setup, the bottom of an open rectangular box is split at the center. The side and bottom walls move in opposite directions, each at $u_s=0.01$ m/s along the split. Periodic boundaries are applied in the shear direction. While the shear band is in many ways similar to that in the circular split-bottom cell, the shear band in the parallel split-bottom cell is symmetric and the center of the shear band at all depths is located at the center plane of the cell [Fig. 2(c)]. Using this in conjunction with the circular split-bottom cell allows us to investigate the effect of curvature on segregation. Several trial runs were performed where the width L_y and length L_x were varied to ensure that system size effects are eliminated. Based on our results and those described in Ref. [38], we chose $L_y=50$ mm and $L_x=21$ mm.

In both the circular and parallel split-bottom cell, a layer of small particles is "glued" to the bottom, as in the physical experiment, to control boundary friction. We fill both cells to a height $H=30$ mm. To save computational cost the shear rates are increased slightly from that of the experiments. In the circular cell, $\Omega=0.15$ rad/s (~2.4 times the rotating speed of experiments). In the parallel cell, the two halves of the cell move in opposite direction to one another at a relative speed of 0.02 m/s. While not exactly comparable, this is similar to the relative speed of the two base parts at the split for the simulation of the circular cell (~0.018 m/s). A few computational experiments performed at different shear speeds lead us to believe that inertial effects are unimportant and therefore that, aside from the rate of segregation, the shear rates do not effect our results. For the circular cell, we denote the velocity and components as $\mathbf{u}=u_i\theta+v_i\mathbf{r}+w_i\mathbf{z}$, and for the parallel cell, we denote them as $\mathbf{u}=u_i\mathbf{x}+v_i\mathbf{y}+w_i\mathbf{z}$, both according to the directions noted in Fig. 2.

A. Circular split-bottom cell

Figure 3 shows snapshots of segregation patterns at the beginning ($t=0$ s) and end ($t=400$ s) of the computational experiment in the circular split-bottom cell. Both a vertical plane and several horizontal planes at different heights z are shown. One can see that segregation patterns similar to the experiments emerge, albeit over a significantly quicker time frame. Large particles segregate to the top and away from the bottom. Away from either surface, horizontal segregation patterns emerge, where small particles accumulate at smaller radii, and larger particles accumulate at larger radii. The dashed lines indicate the centers of shear zone calculated using Equation [1]. Similar to the experimental results, the small particles become highly concentrated at smaller radii, the larger particles become concentrated at larger radii, and a mixed phase exists at the largest radii. Unlike the experiments, the center of the shear zone R_c (dashed lines in the figure) does not separate the zones of high and low concentrations of large particles, though the larger particles seem most highly concentrated at $r>R_c$. This is somewhat different than the experimental observations. The difference may be related to the effect of the inner wall and is currently under investigation.

To study the kinematics that drives this horizontal segregation, we choose a horizontal slice between $z=14$ and 20 mm where the most striking horizontal segregation pattern emerges. In Fig. 4, we plot some of the relevant kinematics for the particles in that slice as a function of radial position during the first 10 seconds (left column) and last 10 seconds (right column) of the simulation.

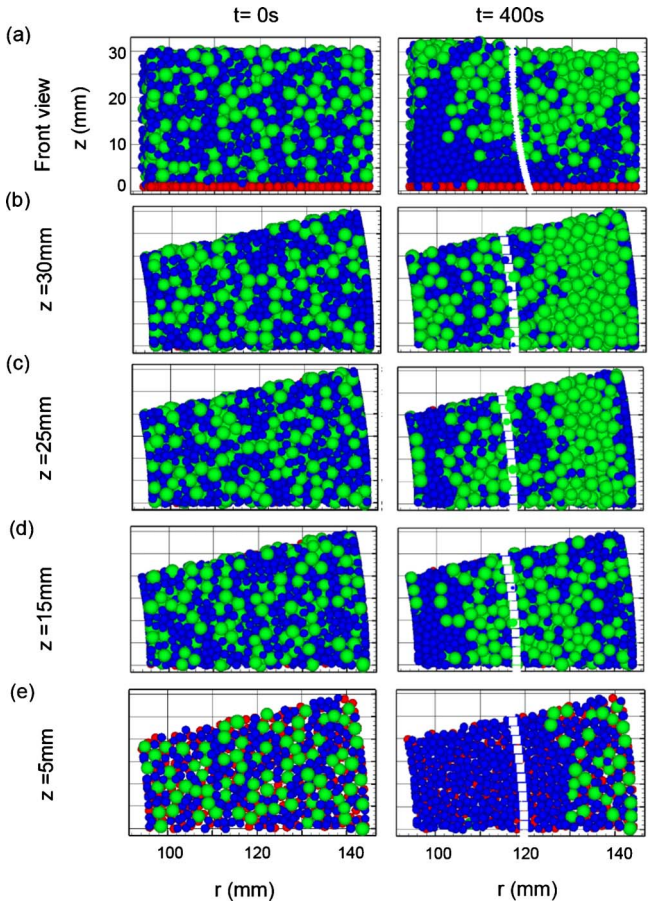

FIG. 3. (Color online) Vertical and horizontal cross sections from computational experiments using 2 mm (dark or blue online) and 3 mm (light, or green online) particles in a circular cell. First column: the beginning of the computational experiment when the particles are well mixed at $t=0$ s. Second column: after $t=400$ s of rotation of the base. (a) Vertical cross section at $\theta=0$. (b)–(e) Horizontal cross sections at heights indicated. The dashed lines indicate the theoretical centers of shear zone, as calculated by Eq. (1). The total filling height H is 30 mm with a glued layer of 2 mm glass particles at the bottom.

Figure 4(a) shows the profiles of solid volume fraction $\bar{f}_i$, where the subscript i represents the particle type or phase: small particles only ($i=1$), large particles only ($i=2$), and the mixed phase ($i=$mix). (Here and henceforth, $\bar{q}_i$ represents a temporal and spatial average of quantity q). One can see from these plots that the concentrations apparent by eye in the snapshots in Fig. 3 are well represented by these plots. At the beginning of simulation, $\bar{f}_i$ is constant across the cell indicating a good mixture. At the end of the simulation, $\bar{f}_1$ is high close to the inner wall indicating there is a high concentration of small particles in this region, and $\bar{f}_2$ is high in the outer part shear zone indicating there is a high concentration of large particles in the part of shear zone close to

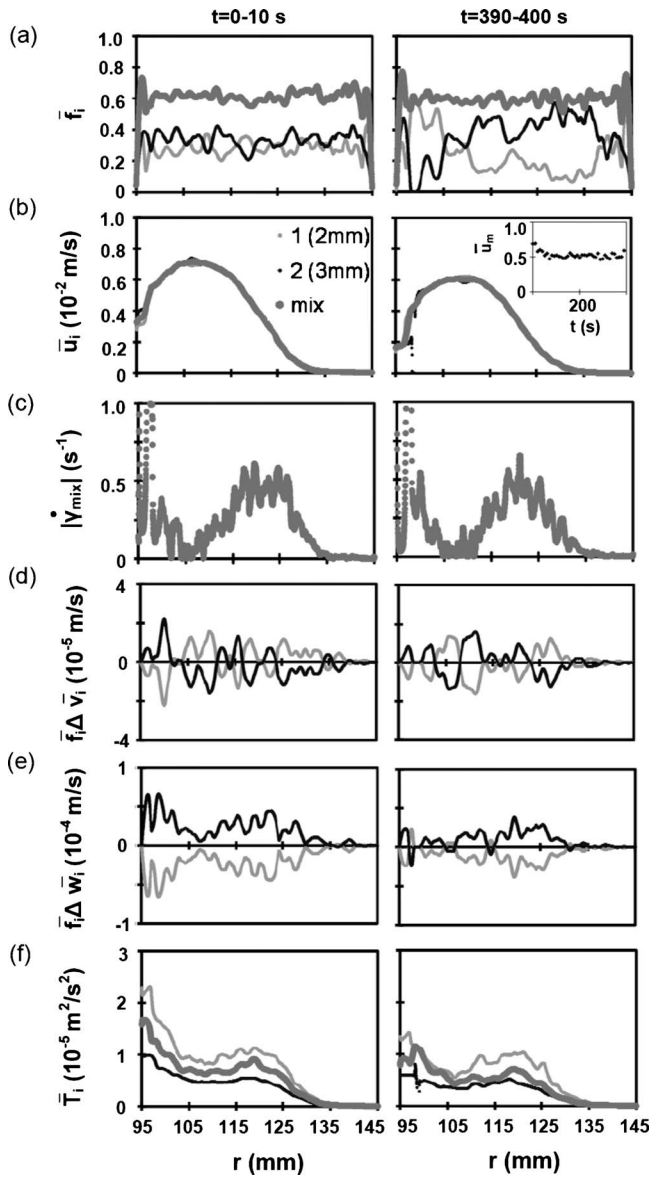

FIG. 4. Kinematics from the computational experiments in the circular cell pictured in Fig. 3. Results shown are from a horizontal slice of the material between $z=14$ mm to 20 mm (approximately halfway between the bottom and the top of the mixture). The kinematics shown are averaged over the first and last ten seconds of the computational experiment: $t=0-10$ s (first column), $t=390-400$ s (second column). The data are averaged in the θ and z directions for each value of r. (a) Solid volume fraction $\bar{f}_i$ (b) Streamwise velocity $\bar{u}_i$. (c) Absolute value of shear rate of mixture $|\dot{\gamma}_{mix}|=|rd(\bar{u}_{mix}/r)/dr|$. (d) Relative flux of particles in the radial direction $\bar{f}_i\Delta\bar{v}_i$. (e) Relative flux of particles in the vertical direction $\bar{f}_i\Delta\bar{w}_i$. (f) Kinematic granular temperature $\bar{T}_i$.

outer wall. There is a narrow mixed region immediately adjacent to the outer wall. After the system has been rotated for some time, there is a subtle dip in the average solids fraction $\bar{f}_{mix}$, similar to that associated with the dilatancy reported in Ref. [39].

Figure 4(b) shows the profiles of the streamwise velocities $\bar{u}_i$ showing, within the central shear zone, a similar curve to that reported previously [28] centered around $R_c \approx 118$ mm. There is significant slip near the inner wall giving rise to an additional shear gradient at the inside wall. Initial transients decrease over the first 50 seconds as shown in the inset where the maximum velocity of the mixture $\bar{u}_m$ is plotted as a function of time. A comparison of the plots for $\bar{u}_i$ [Fig. 4(b)] and shear rate $|\dot{\gamma}_i|=|rd(\bar{u}_i/r)/dr|$ [Fig. 4(c)] with those of $\bar{f}_i$ indicates that the region of a higher concentration of large particles is centered around the highest shear rate, though the widest region that has a consistently higher concentration of large particles is at higher radial positions $r > R_c$.

Figures 4(d) and 4(e) show the profiles of the relative fluxes in the radial and vertical directions: $\bar{f}_i\Delta\bar{v}_i=\bar{f}_i(\bar{v}_i-\bar{v}_{mix})$ and $\bar{f}_i\Delta\bar{w}_i=\bar{f}_i(\bar{w}_i-\bar{w}_{mix})$, respectively. The radial fluxes are notably small and noisy for both small and large particles at the beginning and end of the computational experiment. This indicates there is little or no segregation flux parallel to the shear gradient driving the horizontal segregation pattern. In contrast, the vertical segregation fluxes $\bar{f}_i\Delta\bar{w}_i$ are prominent and consistent. The flux of large particles is upward relative to the mixture and the flux of the small particles is downward. The flux in a region near the inner wall decreases significantly by the end of the experiment while the flux in the region within the shear band decreases but not as much by the end of the experiment.

Figure 4(f) shows the averaged profile of what one might call the "*kinematic* granular temperature" T_i, essentially the velocity variances of the system. $T_i=(u_i'^2+v_i'^2+w_i'^2)/3$, where q_i' is the fluctuation of the quantity of interest q, i.e., $q_i'=q_i-\bar{q}$. For all positions, the kinematic temperature of the smaller particles is greater than that of the large, previously explained for dense granular systems in Ref. [40]. The magnitude of $\bar{T}_i$ is largest near the inner wall where there is significant slip shearing of the particles and in the center of the shear zone.

To investigate the temporal evolution of the solids fraction and fluxes for the whole simulation, we calculate these quantities throughout the entire experiment and average them in the radial direction (as well as the z and θ directions) over ten-second intervals. For quantity q we denote these averages over intervals in time and all three spatial dimensions by $\langle\bar{q}\rangle$. For layers close to free surface ($z=24-30$ mm) and bottom ($z=2-8$ mm) where there appears to be no horizontal segregation structure, we average these quantities over the entire layer, (from $r=R_i$ to R_o). To capture the horizontal segregation in the bulk, we divide the middle layer ($z=14-20$ mm) into two parts according to the boundary between the two segregated shells of large and small particles, indicated in Fig. 4(a) as $r=r^* \approx 105$ mm. Then we calculate two sets of averages in this layer, one from $r=R_i$ to r^*, and the other from $r=r^*$ to R_o. Figure 5 shows the results of these calculations for $\langle\bar{f}_i\rangle$ (first column) $\langle\bar{f}_1\Delta\bar{v}_1\rangle$, and $\langle\bar{f}_1\Delta\bar{w}_1\rangle$ (second column).

The first row shows the data averaged over the top 6 mm of the particles. Figure 5(a) shows that, as expected from observations, the concentration of large particles at the top increases over the course of the experiment, and the concen-

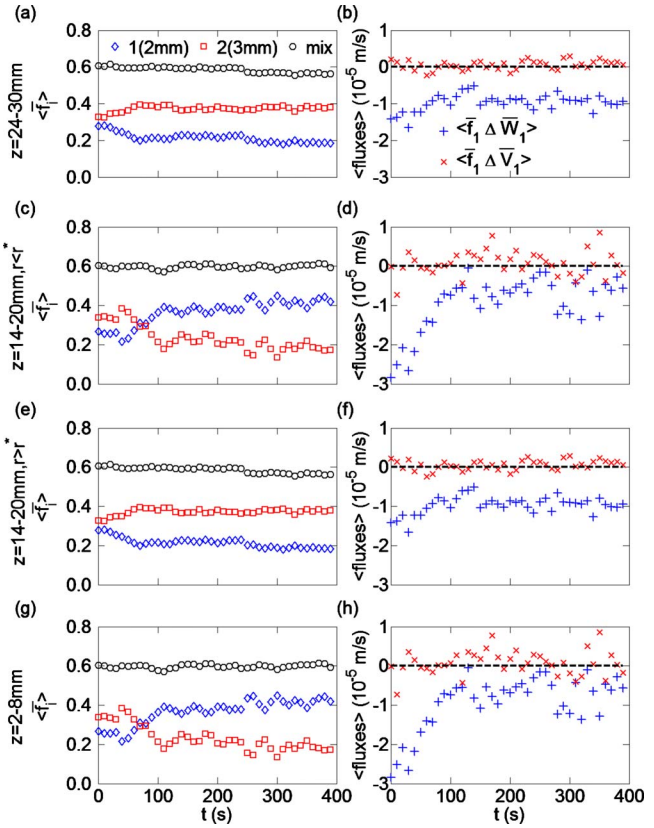

FIG. 5. (Color online) Temporal evolution of the averaged solids fraction and the segregation fluxes at different heights z. The first column shows the averaged solid fraction $\langle \bar{f}_i \rangle$. The second column shows averaged vertical $\langle \bar{f}_1 \Delta \bar{w}_1 \rangle$ and radial $\langle \bar{f}_1 \Delta \bar{v}_1 \rangle$ segregation fluxes for the 2 mm particles. For the top and bottom 6 mm (shown in the first and last row, respectively), the results are averaged over the entire layer. For the middle layer, we plot the results averaged over the smaller radii $(r_1, r_2) = (R_i, r^*)$ in Figs. 5(c) and 5(d) and the results averaged over the larger radii $(r_1, r_2) = (r^*, R_o)$ in Figs. 5(e) and 5(f). $r^* = 105$ mm.

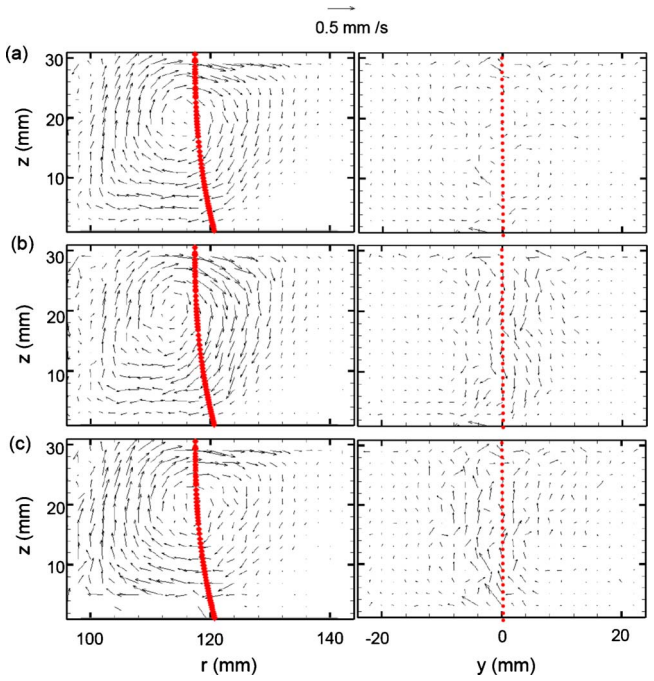

FIG. 6. (Color online) Velocity vectors in a vertical plane perpendicular to the streamwise direction, averaged in the stream-wise direction between $t = 10$ s and 30 s. The first column shows the velocity field of the circular split-bottom geometry, and the second column shows the velocity field of the parallel split-bottom geometry. (a) Results for the mixture. (b) Results for the 2 mm particles. (c) Results for the 3 mm particles.

tration of small particles decreases. The plots of the fluxes of the small particles in Fig. 5(b) show the small particles are moving down relative to the mixture and that there is no net relative horizontal flux in this layer.

The second row contains data from the inner part $(R_i < r \leq r^*)$ of the horizontal slice in the middle of the cell ($z = 14-20$ mm), where the concentration of small particles becomes relatively high [Fig. 4(a)]. The concentration of small particles in this region grows and saturates, and that of the large particles decreases and saturates. Somewhat surprisingly in light of the existence of a horizontal concentration gradient, the horizontal flux remains essentially zero during the entire simulation, while the vertical flux is nonzero initially and then decreases to zero [Fig. 5(d)]. The third row contains the data for the outer part $(r^* \leq r < R_o)$ of the horizontal slice in the middle of the cell ($z = 14-20$ mm), where the concentration of small particles is relatively low. In this region, too, the horizontal flux remains essentially zero, while the vertical flux is nonzero and remains so even though the segregation concentrations seem to stabilize.

The last row shows the data averaged over the bottom 6 mm of the cell. The plots of $\langle \bar{f}_i \rangle$ show that, as expected from observations, the concentration of small particles increases and saturates over the course of the experiment, and the concentration of large particles decreases. The plots of $\langle \bar{f}_1 \Delta \bar{v}_1 \rangle$ and $\langle \bar{f}_1 \Delta \bar{w}_1 \rangle$ show the small particles are moving down slightly relative to the mixture, but only at the very beginning of the experiment, and that there is a slightly positive horizontal flux in this layer.

To summarize these results, both vertical and horizontal segregation patterns are observed in the concentration profiles and in the evolution in the concentration over time. There is a clear vertical (downward) flux of the smaller particles relative to the large until the particles are segregated associated with the vertical segregation pattern. There appears to be two regions of vertical segregation at different radii. One is likely influenced by the inner wall and quickly decays early in the computational experiment [Fig. 5(d)] and one that persists within the bulk over the entire course of the experiment [Fig. 5(f)]. In contrast, there is no clear radial flux of one species relative to the other corresponding to the horizontal concentration segregation pattern.

In lieu of a noticeable horizontal flux driving the horizontal segregation pattern in the circular cell, a second possible "driving force" for the horizontal segregation patterns becomes clear when we plot the velocity vectors in a vertical plane as in Fig. 6. In these plots, we can see a stable vertical convection roll exists in the system. This convective roll per-

sists during the entire duration of the simulation for both mixtures and monosized systems (not shown). The convective roll carries all particles upward at the inner wall, outward at the top surface, downward at the outer part of the shear band, and inward at the bottom of the cell. The dotted lines superposed on the figures show that R_c [calculated using Eq. (1)] cuts nearly through the middle of the convection roll. We believe this convection roll superposed with the relative vertical flux of the particles is responsible for the horizontal segregation pattern.

The process we believe leads to the horizontal segregation pattern is as follows. Wherever large and small particles coexist in the bulk, the large particles rise and the small particles sink. The net rotation of the system causes the large particles segregated at the top to be advected downward along the outside edge of the cell and the small particles segregated at the bottom to be advected upward along the inside edge of the cell. In this way, the large and small particles appear horizontally segregated in the bulk. Particles in these neighboring disparate regions then mix horizontally due to ordinary diffusion in the shear band. In the steady state, this keeps a mixed region in the middle leading to a vertical segregation flux in the shear zone that persists over the duration the experiment [as in Fig. 5(f)].

We believe the convection roll is driven by the circular motion of the particles in the circular cell. This is supported by our results from the parallel cell, as we discuss in the next section.

B. Parallel split-bottom cell

We plot the velocity vectors for the parallel split-bottom cell in the second column of Fig. 6. In contrast to the results from the computational experiments in the circular split-bottom cell, we do not see a vertical global convection roll in the parallel cell. This is independent of the time over which the results are averaged (for the results shown in Fig. 6, the results were averaged over 20 s). While some local convection is apparent over short periods as observed in monosized systems by Ries *et al.* [38], we do not find any long-lasting velocity or vorticity trends in this system. This supports the conjecture that the convection roll observed in the circular cell is due to the curvature and rotation effects. Without the convection roll we can better investigate the effects of the shear gradient.

Figure 7 contains snapshots of segregation patterns at the beginning ($t=0$ s), middle ($t=60$ s), and end ($t=200$ s) of the computational experiment in the parallel cell. Results from a vertical plane and several horizontal planes at different heights z are shown at each of these time steps. As in the circular cell, vertical segregation occurs quickly, where large particles accumulate close to the free surface and small particles accumulate close to the bottom. Additionally, a slow horizontal segregation pattern can be also observed in the bulk. At $t=60$ s, at approximately $2/3H$ large particles begin to accumulate in the center of shear zone, while small particles accumulate at edges of shear zone. The horizontal segregation patterns become more clear by $t=200$ s. Similar to the results in the circular cell, the vertical thickness of the region where horizontal segregation emerges is thin.

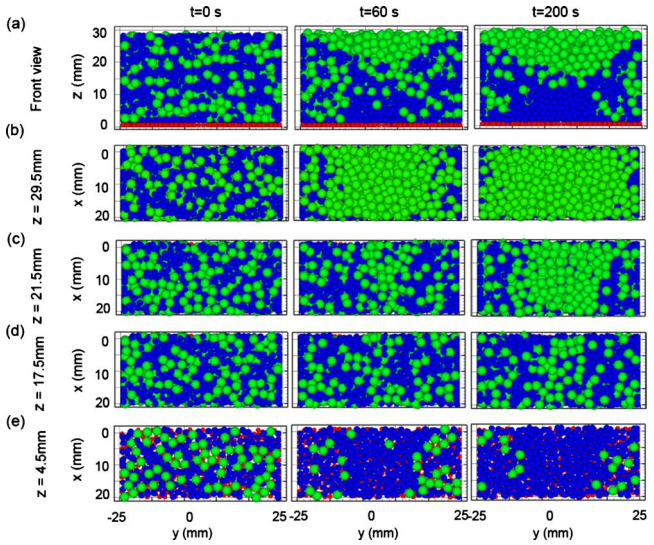

FIG. 7. (Color online) Front and top views from computational experiments in the parallel cell with 2 mm (dark or blue online) and 3 mm (light or green online) particles at the beginning of the computational experiment when the particles are well mixed at $t=0$ s (first column) after $t=60$ s (second column) and after $t=200$ s (third column). (a) Vertical cross section at $x=0$. (b)–(e) Horizontal cross sections at heights indicated. The total filling height H is 30 mm, with a glued layer of 1.5 mm glass particles at the bottom.

In order to investigate this horizontal segregation pattern more quantitatively, we process data within a horizontal slice at $z=13.5-17.5$ mm. In Fig. 8 we plot the profiles of $\bar{f}_i$, $\bar{u}_i$, $\bar{f}_i\Delta\bar{v}_i$, and $\bar{f}_i\Delta\bar{w}_i$, as a function of y for this slice using same method as described for the circular cell.

The plots for $\bar{f}_i$ [Fig. 8(a)] show that the well-mixed system of particles at $t=0$ s evolves to one quite segregated in the horizontal direction by $t=200$ s. Again, the region high concentration of large particles is centered on the point of highest shear rate, while small particles are concentrated at the outer edges of the shear zone. The plots for the azimuthal velocities $\bar{u}_i$ [Fig. 8(b)] again shows the characteristic error function seen in these systems, essentially the same for all particles and at all times. In this case, the highest shear rate is in the center of the cell [Fig. 8(c)]. In contrast with those for the circular cell, the plots for $\bar{f}_i\Delta\bar{v}_i$ [Fig. 8(d)] show a subtle trend of horizontal flux of the large particles into the shear zone at the beginning of the experiment which decays by $t=200$ s. The plots for $\bar{f}_i\Delta\bar{w}_i$ [Fig. 8(e)] show a more dramatic segregation effect in the vertical direction, approximately twice the flux in the horizontal direction. This, too, dies down significantly after 200s. $\bar{T}_i$ [Fig. 8(f)] is biggest where the shear rate is the greatest as in the circular cell, though in this case there is very little slip at the walls, so the $\bar{T}_i$ is significant only in the central shear zone.

To investigate the evolution of the kinematics over time, as for the circular cell, we plot the averaged solid fraction and relative fluxes as a function of time for the parallel cell as we did for the circular cell. For the horizontal flux we take advantage of the symmetry in the problem and calculate the

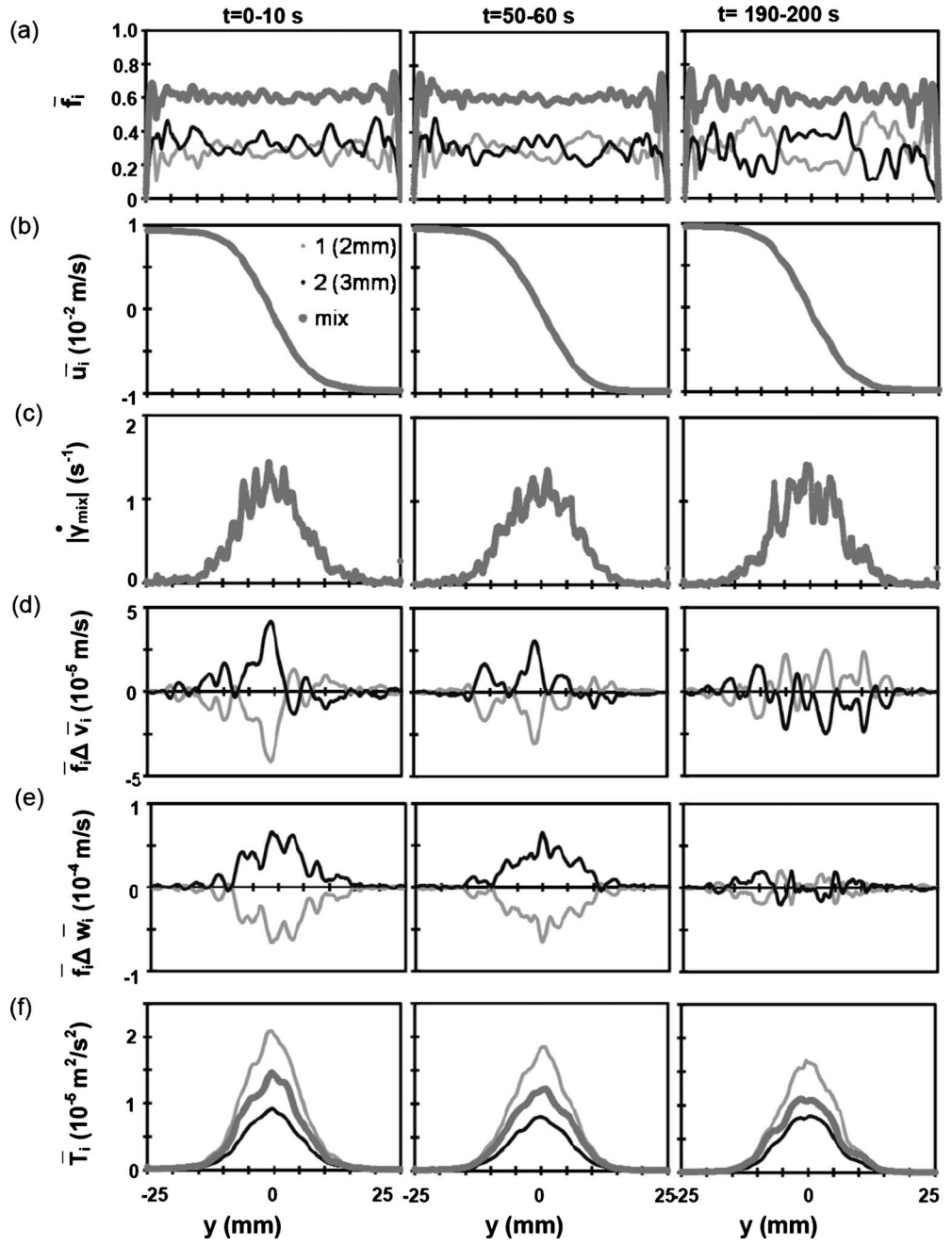

FIG. 8. Kinematics from the computational experiments in the parallel cell pictured in Fig. 7. Results shown are for a horizontal slice of the material between $z=13.5$ mm to 17.5 mm (approximately halfway between the bottom and the top of the system) and averaged in the x and z directions for each value of y. The kinematics are averaged over ten seconds at three different times during the simulation: $t=0-10$ s (first column), $t=50-60$ s (second column), $t=190-200$ s (third column). (a) Solid volume fraction $\bar{f}_i$. (b) Streamwise velocity $\bar{u}_i$. (c) Absolute value of shear rate of mixture $|\dot{\gamma}_{mix}|=|d\bar{u}_{mix}/dy|$. (d) Relative flux of particles in the horizontal direction $\bar{f}_i\Delta\bar{v}_i$. (e) Relative flux of particles in the vertical direction $\bar{f}_i\Delta\bar{w}_i$. (f) Kinematic granular temperature $\bar{T}_i$.

difference between the flux on the left of the cell and that on the right side of the cell: $\langle\bar{f}_1\Delta\bar{v}_1\rangle=\langle\bar{f}_1\Delta\bar{v}_1\rangle_{y<0}-\langle\bar{f}_1\Delta\bar{v}_1\rangle_{y>0}$. By this definition, a positive value of $\langle\bar{f}_1\Delta\bar{v}_1\rangle$ indicates the small particles are moving to the region of highest shear in the center of shear zone. We calculate these quantities for the central 40 mm of our cell and plot them in Fig. 9. The first row shows the data averaged over the top 4 mm of the system of particles; the second row shows the data averaged over the middle 4 mm, and the third row shows the data averaged measured the bottom 4 mm, just above the particles fixed to the base.

The plots of $\langle\bar{f}_i\rangle$ show that, as expected from observations, the concentration of large particles increase near the top of the cell over the course of the experiment, and the concentration of small particles increase near the bottom. The plots of the vertical fluxes of the small particles $\langle\bar{f}_1\Delta\bar{w}_1\rangle$

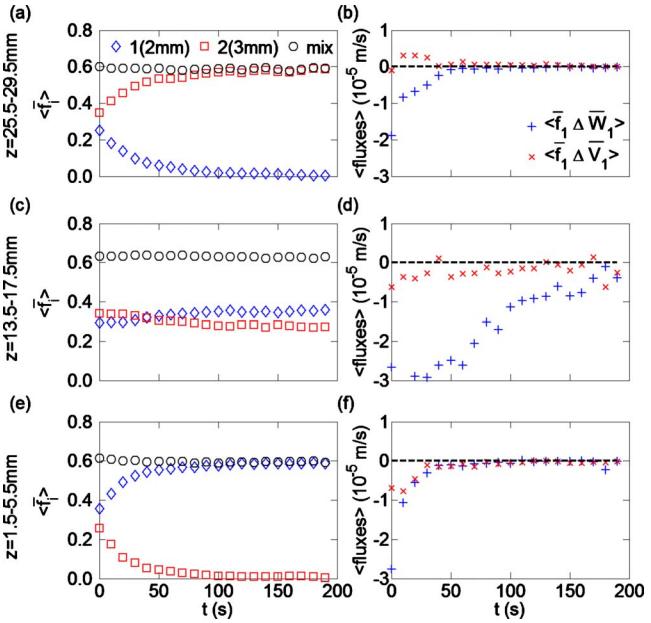

FIG. 9. (Color online) Temporal evolution of the averaged solids fraction and the segregation fluxes at different heights z. The first column shows the averaged solid fraction $\langle \bar{f}_i \rangle$. The second column shows averaged vertical $\langle \bar{f}_1 \Delta \bar{w}_1 \rangle$ and transverse $\langle \bar{f}_1 \Delta \bar{v}_1 \rangle$ segregation fluxes for the 2 mm particles. $\langle \bar{f}_i \rangle$ and $\langle \bar{f}_1 \Delta \bar{w}_1 \rangle$ are averaged over the entire layer. $\langle \bar{f}_1 \Delta \bar{v}_1 \rangle = \langle \bar{f}_1 \Delta \bar{v}_1 \rangle_{y<0} - \langle \bar{f}_1 \Delta \bar{v}_1 \rangle_{y>0}$.

show the small particles are moving down relative to the mixture throughout the system. This trend is short-lived at the top (which quickly becomes depleted of small particles) and at the bottom (which quickly becomes depleted of large particles). The trend is longer lasting in the middle until the remainder of the small particles move from top to bottom, and the remainder of the large particle move from bottom to top. The horizontal fluxes $\langle \bar{f}_1 \Delta \bar{v}_1 \rangle$ are an order of magnitude smaller than the vertical fluxes, yet there is a consistent trend. Throughout the bulk, until segregation is complete, $\langle \bar{f}_1 \Delta \bar{v}_1 \rangle < 0$, indicating the flux of the small particles is on average away from the region of high shear. At the very top surface the trend appears to be slightly reversed, possibly due to the lower solids fraction in this region.

While there is no component of gravity in this horizontal direction, there are a number of other possible driving forces that could give rise to this segregation flux including gradients in the shear rate, the granular temperature, and the solids fractions, and associated pressure gradients. Kinetic theory has the capacity to account the effects of all of these. In the next section we compare predictions from the adaptations of kinetic theory closest to those of our system (e.g., particles are allowed to be dissipative) for insights into this shear-associated segregation.

IV. KINETIC THEORY AND SHEAR-INDUCED SEGREGATION

To compare our results with those predicted by kinetic theory, we use the model derived from kinetic theory described in Ref. [17], which allows the particles to be slightly dissipative and allows for the nonequipartition of temperature between the species. We include the effect of nonequipartition of temperature (e.g., Refs. [16,40–42]) according to expressions in [17] (similar to those in Ref. [16]).

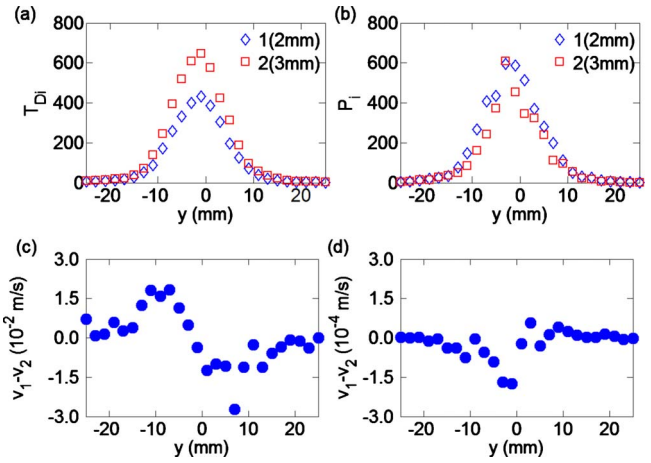

FIG. 10. (Color online) Results from the middle horizontal slice ($z=13.5-17.5$ mm) of the parallel split-bottom cell averaged over $t=0-10$ s. The data shown here are analyzed in the context of kinetic theory considering the nonequipartition temperature of the particles. (a) The dynamic granular temperature for each component $T_{Di}=m_i T_i$. (b) The dynamic granular pressure for each component. (c) Predicted diffusion velocity between small and large particles according to predictions from kinetic theory, detailed in the Appendix. (d) Actual diffusion velocity difference calculated from the DEM simulation results.

We consider the horizontal plane section in the vertical center of the split cell, away from the effects of the boundary, and average the details in the z-direction from $z=13.5$ mm-17.5 mm and across the entire cell in the x direction over the first 10 s of the experiment (as in the first column in Fig. 8). The granular temperature used here is what might be considered a *dynamic* granular temperature compared with the temperature plotted in Figs. 4 and 8: $T_{Di}=m_i T_i$. We plot T_{Di} for both species across the middle horizontal section of the parallel cell in Fig. 10(a). The larger particles have a greater dynamic granular temperature than the smaller particles for all positions in the cell, and for both types of particles the granular temperature is largest in the middle of the cell, consistent with Ref. [40]. The *dynamic granular pressure* for each species P_i [43] accounting for the nonequipartition of granular temperature is calculated by $P_i = n_i(T_{Di}+\Delta T_{Di}) + \Sigma_{k=1}^{2} K_{ik}[T_{Di} + (m_i \Delta T_{Dk} + m_k \Delta T_{Di})/(m_i+m_k)]$: where n_i is the local number density of species i, m_i is the mass of species i, and ΔT_{Di} is the difference between the local temperature of species i and that of the mixture $\Delta T_{Di} = T_{Di} - T_{Dmix}$. K_{ik} is a coefficient concerning the local frequency of interaction between species i and k defined by $K_{ik} = (\pi/3) g_{ik} r_{ik}^3 n_i n_k (1+e)$, where g_{ik} is the radial distribution function between contacting pairs (approximated according to details in Ref. [44]), and e is the coefficient of restitution, which we take here to be $e=0.9$ as in our simulations. The pressure for each species P_i is plotted in Fig. 10(b). It is quite similar for both species and, like the granular temperature, peaks at the center of the shear band.

From considerations associated with momentum conservation, a prediction for the relative segregation velocities of the two components $v_1 - v_2$ may be derived as a function of the dynamic temperatures, dynamic pressures, and ordinary diffusion of the components (see the Appendix). The results for our computational split-bottom cell are plotted in Fig. 10(c). For $y<0$, $v_1-v_2>0$, and for $y>0$, $v_1-v_2<0$, which indicates that the small particles will move to center of shear zone relative to the large particles. The actual difference in measured segregation velocities is plotted in Fig. 10(d). The measured segregation velocity difference is smaller (by approximately two orders of magnitude) and in the opposite direction compared with that predicted by kinetic theory. In other words, the theory predicts that large particles segregate to the region of lowest dynamic temperature and pressure. For our system large particles actually segregate to the region of higher dynamic temperature and pressure. While there are slightly different formulations predicting segregation in the framework of kinetic theory, those that include effects associated with slightly dissipative particles and that allow for different species temperatures (e.g., [16,17]) lead to the same results.

Our conclusions from this are twofold. First, we find the differences between the predictions from kinetic theory and our computational results indicative of the importance of the nature of the bulk dynamics in determining the form of segregation. The framework of kinetic theory most readily available is based on assumptions that the particle interactions are binary and near-instantaneous, whereas in our system particle contacts are multiple and enduring. It is, therefore, not surprising that different segregation effects arise from these different system dynamics; our results point to the importance of these interactions in determining the segregation details. In other words, rather than indicate that there is some failing in kinetic theory, our results indicate that in fact there is a significance in what might be considered these different "phases" of sheared granular systems that affects the nature of the shear-driven segregation.

Our second set of conclusions from this analysis regards some assumptions within the framework of kinetic theory closest to dense sheared granular flow. One modification that may improve the predictions of kinetic theory for denser sheared systems like the split-bottom cells could involve the radial distribution function. Its current form is based on a system where binary collisions dominate the interparticle interactions. As we have discussed, this is not the case for our mixtures sheared in split-bottom cells where inertial effects appear negligible. Perhaps if the radial distribution function were modified to account for effects associated with systems such as these, kinetic theory would better reproduce the segregation dynamics in denser flows such as those we study in the split-bottom cell.

V. CONCLUSIONS

In summary, we use a split-bottom cell to study segregation experimentally and computationally, with an emphasis on determining the origin of horizontal segregation patterns apparently associated with a horizontal shear gradient in these systems. In both the physical and computational experiments we observe both horizontal and vertical segregation patterns. In both the circular and parallel split-bottom simulated cells, vertical fluxes of large particles upward and small particles downward lead to vertical segregation patterns at the top and bottom of the cells. However, it appears the underlying driving mechanism for the horizontal segregation pattern is different for the two types of cells. In the circular cell, while there may be the tendency for small horizontal segregation fluxes, the effects are suppressed by the more prominent dynamics associated with the convection roll causing *all* particles to rise in the middle at smaller radii and to sink on the outside at larger radii. These have the effect of rotating a vertical segregation pattern (that is likely driven by gravity) outward leading to a net horizontal segregation pattern. These observations suggest what appears to be some contradictory results for shear-induced segregation in dense flows may in fact be due to a combination of other segregation effects and particle advection. In the parallel split-bottom cell, no global convection roll is observed. In this case, a small horizontal flux is apparent of small particles away from the highest shear rate and highest granular temperature, and large particles tend to move inward.

We use expressions derived within the framework of kinetic theory to determine whether or not the horizontal segregation velocities observed in the parallel cell are associated with pressure and temperature gradients derived from the measured kinematics. We find the theoretically predicted segregation velocities to be much larger and in the opposite direction to those measured in the simulations. We believe these differences are associated with the nature of the interparticle collisions and their influence on segregation trends. Granular mixtures whose dynamics are dominated by near-instantaneous binary collisions appear to segregate differently than those whose dynamics are dominated by multiple enduring contacts with their neighbors. On the other hand, this form of kinetic theory may be applicable to horizontal segregation at the very top of these split-bottom systems where the particles are more sparse, and interparticle collisions may be more important in the dynamics. Indeed, the results from the top of our computational experiments in the parallel cell indicate the segregation fluxes in this region are opposite to those observed in the bulk [Fig. 9(b)]. Additional experiments where a higher degree of precision is attained would be helpful in determining whether or not this is the case.

Alternatively, recent theory proposed by Sarkar and Khakhar [45] shows promise in an alternate model for segregation arising from shear gradients in dense granular flows. They demonstrated that an effective temperature derived from the fluctuation-dissipation relation could be used to predict segregation fluxes for binary mixtures differing in material density in a rotating drum. This effective temperature is a function of local viscosity and diffusivity both functions of local shear rate. While the current version of the model only has the capacity to consider particle density differences (not size differences) in a mixture, the framework shows promise for eventually predicting size segregation associated with shear rate gradients as well.

ACKNOWLEDGMENTS

We are grateful for helpful discussions with Prof. James Jenkins and for the financial support of NSF under Grants No. NSF CMS-0625022 and No. NSF CBET-0932735. This work was carried out in part using computing resources at the University of Minnesota Supercomputing Institute.

APPENDIX: CALCULATIONS RELATED TO KINETIC THEORY SEGREGATION PREDICTIONS

As in Refs. [9,12,16] we consider the predictions from kinetic theory in the form of the following equation:

$$v_1 - v_2 = -\frac{n^2}{n_1 n_2} D_{12}(d_1). \tag{A1}$$

In this expression, the subscripts 1 and 2 refer to the small and large species, respectively. $v_1 - v_2$ represents the diffusion velocity of the small particles relative to that of the large particles – for these results in the positive y direction [see Fig. 2(b)]. The total local number density $n = n_1 + n_2$. D_{12} is the local coefficient of ordinary diffusion defined by

$$D_{12} = \frac{n_1 n_2}{n} \frac{r_1 + r_2}{K_{12}} \left(\frac{\pi (m_1 + m_2) T}{32 m_1 m_2} \right)^{1/2}. \tag{A2}$$

Finally, d_1 (sometimes called a "diffusion force" [13]) represents competing segregation and mixing factors leading to the difference in diffusion velocities between the two types of particles: $v_1 - v_2$. Similar to Ref. [16] we express in terms of three components,

$$d_1 = d_{P12} + d_{T12} + d_{n12}, \tag{A3}$$

where the segregation and mixing factors related to granular pressure, temperature, and ordinary diffusion are represented by d_{P12}, d_{T12}, and d_{n12}, respectively. Specifically

$$d_{P12} = \frac{\frac{P_2}{P_1} \nabla P_1 - \nabla P_2}{nT \left(\frac{P_2}{P_1} + 1 \right)}, \tag{A4a}$$

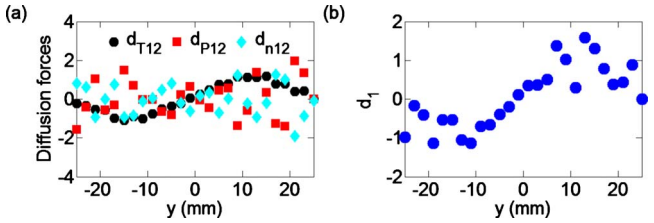

FIG. 11. (Color online) (a) Segregation and mixing "driving forces" associated with dynamic pressure (d_{P12}), dynamic temperature (d_{T12}), and ordinary diffusion (d_{n12}) as defined in the text. (d) Sum of the driving forces associated with segregation and mixing: $d_1 = d_{P12} + d_{T12} + d_{n12}$.

$$d_{T12} = -\frac{K_{12}}{nT} \frac{m_2 - m_1}{m_2 + m_1} \nabla T, \tag{A4b}$$

$$d_{n12} = -\frac{K_{12}}{n} \left[\frac{\nabla n_1}{n_1} - \frac{\nabla n_2}{n_2} \right]. \tag{A4c}$$

In each case ∇q refers to the gradient of q, the physical quantity of interest (P, T and n). Positive values of each represent interactions leading to a net motion of the small particles in the negative y-direction. Each of Eqs. (A4a) and (A4c) are derived according to the theory in [17]. The form is similar but not exactly identical to the theoretical results in [16]. The predictions for diffusion forces in our system summarized by Figs. 11(a) and 11(b) and segregation velocities [Fig. 10(c)] are essentially the same.

Each of the segregation/mixing forces are plotted in Fig. 11(a). While d_{P12} and d_{n12} are somewhat noisy and do not exhibit a clear trend, d_{T12} exhibits a clear trend, negative on the left side of the shear band, and positive on the right side of the shear band. The sum of these d_1 is plotted in Fig. 11(b). Like d_{T12}, for $y<0$, $d_1<0$ and for $y>0$, $d_1>0$ indicating that the small particles are *forced* into the center of the shear band. As we discuss in Sec. IV, this is opposite to our computational results, suggesting a clear dependence of the segregation trend on the nature of the particle-particle interactions.

[1] J. M. N. T. Gray and A. R. Thornton, Proc. R. Soc. London, Ser. A **461**, 1447 (2005).
[2] J. M. N. T. Gray and V. A. Chugunov, J. Fluid Mech. **569**, 365 (2006).
[3] D. V. Khakhar, J. J. McCarthy, and J. M. Ottino, Phys. Fluids **9**, 3600 (1997).
[4] K. M. Hill, D. V. Khakhar, J. F. Gilchrist, J. J. McCarthy, and J. M. Ottino, Proc. Natl. Acad. Sci. U.S.A. **96**, 11701 (1999).
[5] S. B. Savage and C. K. K. Lun, J. Fluid Mech. **189**, 311 (1988).
[6] D. J. Stephens and J. Bridgwater, Powder Technol. **21**, 29 (1978).
[7] W. S. Foo and J. Bridgwater, Powder Technol. **36**, 271 (1983).
[8] F. Rietz and R. Stannarius, Phys. Rev. Lett. **100**, 078002 (2008).
[9] S. L. Conway, X. Liu, and B. J. Glasser, Chem. Eng. Sci. **61**, 6404 (2006).
[10] J. Liu and A. D. Rosato, J. Phys.: Condens. Matter **17**, S2609 (2005).
[11] H. Xu, M. Louge, and A. Reeves, Continuum Mech. Thermodyn. **15**, 321 (2003).
[12] J. T. Jenkins and F. Mancini, ASME J. Appl. Mech. **54**, 27 (1987).
[13] J. T. Jenkins and F. Mancini, Phys. Fluids A **1**, 2050 (1989).
[14] B. Ö. Arnarson and J. T. Willits, Phys. Fluids **10**, 1324 (1998).
[15] J. T. Willits and B. Ö. Arnarson, Phys. Fluids **11**, 3116 (1999).
[16] J. E. Galvin, S. R. Dahl, and C. M. Hrenya, J. Fluid Mech. **528**, 207 (2005).

[17] D. K. Yoon and J. T. Jenkins, Phys. Fluids **18**, 073303 (2006).
[18] D. Serero, I. Goldhirsch, S. H. Noskowicz, and M.-L. Tan, J. Fluid Mech. **554**, 237 (2006).
[19] D. V. Khakhar, J. J. McCarthy, and J. M. Ottino, Chaos **9**, 594 (1999).
[20] D. Leighton and A. Acrivos, J. Fluid Mech. **177**, 109 (1987).
[21] D. Leighton and A. Acrivos, J. Fluid Mech. **181**, 415 (1987).
[22] J. R. Abbott, N. Tetlow, A. L. Graham, S. A. Altobelli, E. Fukushima, L. A. Mondy, and T. S. Stephens, J. Rheol. **35**, 773 (1991).
[23] G. P. Krishnan, S. Beimfohr, and D. T. Leighton, J. Fluid Mech. **321**, 371 (1996).
[24] C. Barentin, E. Azanza, and B. Pouligny, Europhys. Lett. **66**, 139 (2004).
[25] J. Bridgwater, M. H. Cooke, and A. M. Scott, Trans. Inst. Chem. Eng. **56**, 157 (1978).
[26] I. Zuriguel, J. F. Boudet, Y. Amarouchene, and H. Kellay, Phys. Rev. Lett. **95**, 258002 (2005).
[27] K. M. Hill and Y. Fan, Phys. Rev. Lett. **101**, 088001 (2008).
[28] D. Fenistein and M. van Hecke, Nature (London) **425**, 256 (2003).
[29] D. Fenistein, J. W. van de Meent, and M. van Hecke, Phys. Rev. Lett. **92**, 094301 (2004).
[30] D. Fenistein, J. W. van de Meent, and M. van Hecke, Phys. Rev. Lett. **96**, 118001 (2006).
[31] X. Cheng, J. B. Lechman, A. Fernandez-Barbero, G. S. Grest, H. M. Jaeger, G. S. Karczmar, M. E. Möbius, and S. R. Nagel, Phys. Rev. Lett. **96**, 038001 (2006).
[32] T. Unger, J. Török, J. Kertész, and D. E. Wolf, Phys. Rev. Lett. **92**, 214301 (2004).
[33] P. A. Cundall and O. D. L. Strack, Geotechnique **29**, 47 (1979).
[34] At each time step, the force between two objects in contact is calculated according to $\mathbf{F}=F_n\mathbf{n}+F_t\mathbf{t}$ where $\mathbf{n}$ is normal to the plane of interaction $\mathbf{t}$ is tangential to that plane, and the force components are calculated as follows. $F_n=k_n\delta_n^{3/2}+\eta_n\delta_n^{1/4}V_n$; and $F_t=\min(k_t\delta_n^{1/2}\delta_t+\eta_t\delta_n^{1/4}V_t,\mu\times F_n)$. Here δ_n and δ_t are effective normal and tangential overlaps between contacting objections, and $k_{n,t}$, $\eta_{n,t}$, and μ are defined according to material properties as detailed in [35].
[35] Y. Tsuji, T. Tanaka, and T. Ishida, Powder Technol. **71**, 239 (1992).
[36] To reduce the computational time for the circular cell we reduce the normal stiffness k_n from $O[10^8]mg/d$ as determined from experiments in Ref. [35] to $O[10^5]mg/d$ as in Refs. [31,37]. This reduces the time step by a factor of 10. We compare the kinematics in a parallel split-bottom cell with and without reducing k_n, and we find good agreement in the average kinematics and in the segregation patterns.
[37] M. Majid and P. Walzel, Powder Technol. **192**, 311 (2009).
[38] A. Ries, D. E. Wolf, and T. Unger, Phys. Rev. E **76**, 051301 (2007).
[39] K. Sakaie, D. Fenistein, T. J. Carroll, M. van Hecke, and P. Umbanhowar, EPL **84**, 38001 (2008).
[40] K. M. Hill and J. Zhang, Phys. Rev. E **77**, 061303 (2008).
[41] R. D. Wildman and D. J. Parker, Phys. Rev. Lett. **88**, 064301 (2002).
[42] K. Feitosa and N. Menon, Phys. Rev. Lett. **88**, 198301 (2002).
[43] The dynamic pressure, distinct from the hydrostatic pressure, is derived from considerations within the framework of kinetic theory and continuity of momentum for the two species as shown by Refs. [16,17].
[44] The radial distribution function is approximated as in Ref. [17] by $g_{ik}=1/(1-f)+6r_ir_k/r_{ik}\times\xi/(1-f)^2+8(r_ir_k/r_{ik})^2\times\xi^2/(1-f)^3$, where $r_{ik}=r_i+r_k$, and $\xi=2\pi(n_1r_1^2+n_2r_2^2)/3$.
[45] S. Sarkar and D. V. Khakhar, EPL **83**, 54004 (2008).